

# Full-Scale Experimental Pushover Testing of an Existing URM

## Building

Hogan, L.S.<sup>1\*</sup>, Giongo, I.<sup>2</sup>, Walsh, K.Q.<sup>3</sup>, Ingham, J.M.<sup>4</sup>, and Dizhur, D.<sup>5</sup>

**Abstract:** Due to the large number of existing unreinforced masonry (URM) buildings worldwide, and the significant seismic risk that this building stock represents, it is important to quantify the seismic behaviour of such buildings in order to provide assessment guidance to practicing structural engineers. Current assessment guidelines have received little benchmarking against the results of large scale lateral testing of typical URM buildings. In response, field testing was performed on a decommissioned vintage URM building to investigate the in-situ behaviour of URM piers and compare actual behaviour to that predicted by existing assessment frameworks. The tested building was a prototypical, three-storey, 1930s fired clay brick URM building located in Auckland, New Zealand. A pushover test was performed by applying a load to the roof level of the building with a 22 tonne excavator, resulting in the formation of a pier rocking mechanism consistent with the predicted modes determined using current assessment guidelines for URM piers. Finite element modelling was able to replicate the results of the experimental testing, but a reduction of the masonry elastic modulus when acting in tension was required in order to match experimental force-displacement response. The calibrated finite element model was subjected to a pushover analysis of the entire building and was used to benchmark the ability of common seismic assessment techniques and simplified macro-element models to predict failure mechanism and building capacity. It was found that macro-element models tended to under-predict the capacity of the building unless an artificial rigid diaphragm constraint was introduced, and that current assessment

techniques and 2D macro-element modelling of individual facades provided a dependable lower bound on the capacity of URM frame-type buildings.

**Keywords:** Field testing, full scale pushover test, URM, clay brick, FEM masonry, macro-element, seismic assessment

- 1) *\*Lecturer, Department of Civil and Environmental Engineering, University of Auckland, Auckland, New Zealand*
- 2) *Assistant Professor, Department of Civil, Environmental and Mechanical Engineering, University of Trento, Italy*
- 3) *Director of Resiliency and Sustainability of Engineering Systems & Assistant Teaching Professor, Department of Civil & Environmental Engineering & Earth Sciences, University of Notre Dame, Indiana, United States; and Senior Structural Engineer, Frost Engineering and Consulting, Mishawaka, Indiana, United States*
- 4) *Professor, Department of Civil and Environmental Engineering, University of Auckland, Auckland, New Zealand*
- 5) *Lecturer, Department of Civil and Environmental Engineering, University of Auckland, Auckland, New Zealand*

[lucas.hogan@auckland.ac.nz](mailto:lucas.hogan@auckland.ac.nz), [ivan.giongo@unitn.it](mailto:ivan.giongo@unitn.it), [kwalsh8@nd.edu](mailto:kwalsh8@nd.edu), [j.ingham@auckland.ac.nz](mailto:j.ingham@auckland.ac.nz) and [ddiz001@aucklanduni.ac.nz](mailto:ddiz001@aucklanduni.ac.nz)

*\*Corresponding author*

## **1 INTRODUCTION**

Unreinforced masonry (URM) buildings represent one of the most seismically vulnerable building types, and their prevalence in high seismic areas has resulted in a significant amount of research being undertaken to develop techniques for the performance assessment of these buildings. While this research has provided valuable inputs for the development of these assessment tools, the tests typically represent building components with idealised boundary conditions [1 – 5], and to date comparatively few large scale tests of URM buildings are available to evaluate the existing assessment tools [6 – 7]. In response, monotonic pushover testing was performed on a prototypical URM building scheduled for demolition in Auckland, New Zealand. One elevation of the building was subjected to a point load generated by a 22 tonne excavator at roof level to determine the lateral capacity and failure mechanisms of the tested elevation. This test represents one of the tallest URM buildings ever tested in situ. The results from field testing were used to benchmark existing assessment methodologies as well as benchmark finite element (FE) and macro-element (ME) models to determine the ability of these assessment and modelling techniques to determine the failure mechanism, strength, and stiffness of the building.

## **2 TEST BUILDING DESCRIPTION**

The test building, located at 27 Rutland Street in the Auckland central business district (CBD), was a prototypical unreinforced clay brick masonry building [8 – 9] constructed in 1931. The building had floor dimensions of approximately 10 m in the E-W direction and 12 m in the N-S direction (see Figure 1). The

building consisted of four storeys, with three storeys above grade (approximately 11.3 m from grade to the top of the reinforced concrete (RC) parapet at the north elevation) and a basement level. The primary gravity loadbearing elements of the building consisted of URM piers and walls. A continuous RC bond beam extended around the perimeter of the building at the roof level, on which timber roof trusses were supported. RC bond beams at all other storey levels extended around the perimeter of the building (excluding the east elevation), where the RC beams acted as window lintels. The concrete bond beam on the east elevation lacked any reinforcement, and steel angle lintels were used over the few small openings on the east URM wall.

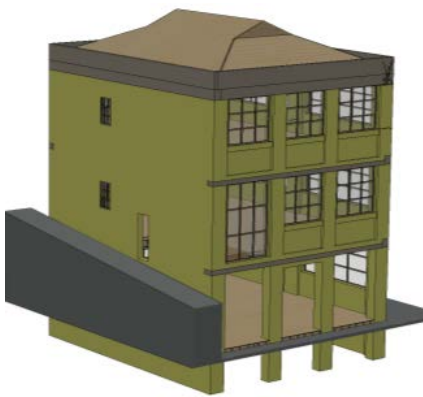
The original floor diaphragm construction consisted of timber joists spanning in the N-S direction, sized primarily 280 mm x 50 mm with an average centre-to-centre spacing of 420 mm. A concrete encased rolled steel joist (RSJ) column was positioned at the centre of the building, supporting a concrete encased steel beam spanning in the E-W direction, which in turn supported the timber joists at all floor levels except at roof level. Tongue and groove timber flooring, with an approximate thickness of 20 mm, was used at all floor levels. The roof of the subject building was supported by three large timber trusses spanning E-W and supporting timber purlins and plank sheathing. The building foundation consisted of shallow RC strip and spread footings supporting URM walls and piers. All interior partition walls and any “false floors” that were installed on top of the tongue and groove flooring were removed prior to testing. No interior URM or load-bearing partition walls were present in the building during pushover testing.



(a) North elevation



(b) West elevation



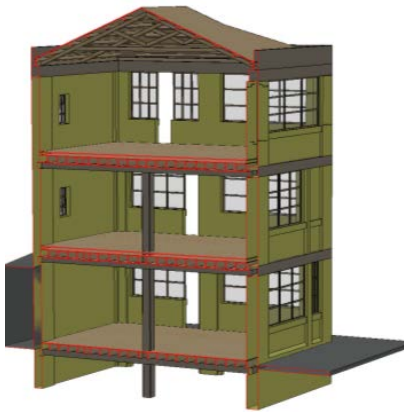
(c) N-E corner



(d) N-W corner



(e) S-E corner



(f) Elevation cross-section



(g) Floor-plan cross-section

Figure 1. The tested building located at 27 Rutland Street, Auckland CBD

## 2.1 Material Properties

Samples were extracted from the test building to quantify the material properties of the masonry, steel reinforcement, and concrete bond beams. The measured properties for these materials are listed in Table 1 alongside the corresponding test standards and other references used to characterise the material. Note that the mean measured mortar compression strength ( $f'_j$ ) of 4.3 MPa would qualify the mortar as “weak” per Kaushik et al. [10] and as mortar of “medium hardness” per NZSEE [11]. By comparison, nearly half of a group of tested samples from 98 pre-1950 buildings in New Zealand had mortar compressive strengths ranging between 0.5 – 2.0 MPa (i.e., “soft” mortar with low cohesion) with a median value near 1.8 MPa [12]. While chemical testing was not carried out on the mortar samples extracted from the test building, based on visual appearance and the mortar compressive strengths measured here it was concluded that lime was present in the mortar mix [2, 12]. The mean measured brick compression strength,  $f'_b$ , of 20.8 MPa and brick rupture strength,  $f'_{br}$ , of 2.8 MPa would qualify the clay bricks as between “soft” and “medium” hardness per NZSEE [11] and Almesfer et al. [12]. This value of brick compressive strength is similar to that found from previous studies of pre-1940 clay-fired brick buildings in New Zealand which had brick compressive strengths ranging between 10 – 20 MPa, with a median value near 17 MPa [12]. The mean measured modulus of elasticity for masonry prisms extracted from the building ( $E_m$ ) was 5632 MPa and was determined using ASTM C1314-11a [13] and TMS [14], as the chord modulus between measured stresses of 0.05 and 0.33  $f'_m$ , where  $f'_m$  represents the masonry prism compression strength. Note that the mean measured value of  $E_m$  in this study was relatively high compared to the mean measured value of  $f'_m$  of 6.2 MPa according to the relationships proposed by

Kaushik et al. [10] and TMS [14]. The mean measured masonry density ( $\rho_m$ ) of 1833 kg/m<sup>3</sup> is consistent with commonly used design assumptions for clay brick masonry in New Zealand [11].

Table 1 also lists the strength and stiffness of a series of compression tests of concrete cylinder cores (tested in accordance with NZS 3112.2 [15]) that were approximately 100 mm in diameter. The mean measured compressive strength of the concrete cores ( $f'_c$ ) was 18.5 MPa. By comparison, Transit New Zealand [16] prescribes a specified nominal compressive strength of 14 MPa for concrete produced up to 1932 and 17 MPa for the period 1933 to 1940 in New Zealand, with a suggested increase in strength due to age ranging from  $1.18(f'_c)$  [17] to  $1.5(f'_c)$  [18 – 19] (i.e. 20 – 25.5 MPa). Hence, the concrete tested in this research program was at the lower bound of expected values.

NZSEE [19] and Transit New Zealand [16] assessment guidelines also serve as references against which to gauge the outcomes of the steel reinforcement material tests, with NZSEE [19] prescribing for analysis a characteristic mean yield strength of 300 MPa and minimum yield strength of 227 MPa (i.e. ASTM grade 33) for steel reinforcement produced as early as 1930. Alternatively, NZSEE [19] recommends that the lower characteristic yield strength be multiplied by 1.08 to approximate the probable yield strength (i.e. 245 MPa for ASTM grade 33). Transit New Zealand [16] prescribes for analysis a characteristic minimum yield strength of 210 MPa for steel reinforcement produced up to 1932 and of 250 MPa for the period 1933 to 1966. Note that, as shown in Table 1, the mean measured tensile yield strengths ( $f'_{sy}$ ) of 267 MPa and 312 MPa for the 10 mm and 12.7 mm diameter samples, respectively, exceed the minimum yield strengths recommended by the New

Zealand guidelines for the time period considered.

**Table 1. Material characteristics of test building located at 27 Rutland Street**

Material characteristic (MPa u.n.o.)	Standards and other references	# samples	Mean	Standard deviation	CV*	
Mortar compression strength, $f'_j$	[20 – 21]	30	4.3	1.5	0.34	
Brick compression strength, $f'_b$	[22]	14	20.8	6.3	0.30	
Brick rupture strength (modulus of rupture), $f'_{br}$		9	2.8	0.55	0.20	
Masonry bed joint shear strength, $f'_{jv}$	[23]	7	0.44	0.11	0.25	
Masonry prism compression strength, $f'_m$	[13 – 14]	4	6.3	1.6	0.25	
Masonry prism elastic modulus, $E_m$		4	5632	2189	0.39	
Masonry prism flexural bond strength, $f'_{fb}$	[24]	2	0.34	0.20	0.58	
Masonry prism density, $\rho_m$ (kg/m <sup>3</sup> )	-	5	1833	110	0.06	
Concrete compressive strength, $f'_c$	[15, 25]	7	18.5	2.4	0.13	
Concrete elastic modulus, $E_c$		6	18,190	3,692	0.20	
Concrete splitting tensile strength, $f'_{ct}$	[15]	5	2.1	0.26	0.12	
Concrete density, $\rho_c$ (kg/m <sup>3</sup> )	[25]	12	2312	38	0.02	
10-mm reinf. steel tensile yield strength, $f'_{sy}$	[26]	4	267	12	0.04	
10-mm reinf. steel tensile yield strain, $\epsilon'_{sy}$ (mm/mm)		4	0.0013	0.0002	0.13	
10-mm reinf. steel tensile ult. strength, $f'_{su}$		5	364	13	0.04	
10-mm reinf. steel tensile strain at ult. strength, $\epsilon'_{su}$ (mm/mm)		4	0.1998	0.0125	0.06	
10-mm reinf. steel elastic modulus, $E_s$		5	208,097	24,661	0.12	
12.7-mm reinf. steel tensile yield strength, $f'_{sy}$		7	312	11	0.03	
12.7-mm reinf. steel tensile yield strain, $\epsilon'_{sy}$ (mm/mm)		7	0.0016	0.0001	0.08	
12.7-mm reinf. steel tensile ult. strength, $f'_{su}$		9	421	31	0.07	
12.7-mm reinf. steel tensile strain at ult. strength, $\epsilon'_{su}$ (mm/mm)		5	0.1728	0.0244	0.14	
12.7-mm reinf. steel elastic modulus, $E_s$		7	200,400	15,972	0.08	
10-mm reinf. steel density, $\rho_s$ (kg/m <sup>3</sup> )		-	5	7792	45	0.01
12.7-mm reinf. steel density, $\rho_s$ (kg/m <sup>3</sup> )		-	7	7767	74	0.01

\*CV = Coefficient of variation

### 3 TESTING METHODOLOGY

Pushover testing of the subject building was simulated using a 22 tonne excavator (see Figure 2). The west elevation of the subject building was selected for testing due to the presence of large window openings on the elevation which formed three load-resisting URM piers that were estimated to have combined capacities less than that of the excavator (see Figure 1 and Figure 2), and for accessibility on site and reduced risk to public spaces. The failure mode and load capacity of the top storey piers was estimated with the current seismic assessment guidelines for URM buildings developed by the New Zealand Society for Earthquake Engineering (NZSEE) [11] and from ASCE 41 [27]. The ultimate capacities for the potential failure mechanisms are shown in Table 2 in which  $V_r$  relates to rocking failure,  $V_{tc}$  relates to toe crushing of the pier,  $V_{dt}$  relates to diagonal tension failure,  $V_s$  relates to bed-joint sliding failure of the piers, and  $V_{r,flanged}$  relates to the rocking failure of the piers while accounting for the flanged geometry of the North and South Piers (see Figure 1). The values for  $V_r$  and  $V_{tc}$  were calculated for two different boundary conditions including: fixity at the top and bottom of the piers ( $\alpha = 1.0$ ); and fixity at the pier base but free to rotate at the top of the pier ( $\alpha = 0.5$ ). While it is common practice to assume fixity at the top and bottom of these piers, the fixed-free case was investigated as a lower bound strength and was used to benchmark against the realistic boundary conditions found in the test building. It was predicted that the URM piers would be subjected to a rocking type failure occurring at a load of 73 kN if the piers exhibited fixity at both their top and base ( $\alpha = 1.0$ ) or at 41 kN if the piers exhibited fixity only at their base ( $\alpha = 0.5$ ) (Table 2).

The presence of flanges on URM piers has been shown to influence their in-plane response. Yi et al. [28] developed a set of formulae to predict the capacity of flanged walls based on internal stress distribution in the URM walls. The primary shear capacities of the piers were calculated according to NZSEE [11] and from ASCE 41 [27] while neglecting the flanges, and the effects of flanges on rocking capacity (the assumed dominant mechanism) were evaluated by considering the flange self-weight acting at the geometrical centroid, with updated values for rocking capacity provided in Table 2. The total capacity of the top level of the tested elevation when accounting for flanged effects was predicted as 80 kN for fixed-fixed piers (cf. 73 kN when neglecting flange effects) or 48 kN for fixed-free piers (cf. 41 kN when neglecting flange effects). As such, the presence of flanges was expected to provide a minimal increase in lateral capacity to the top storey of the building west wall.

**Table 2. Predicted pier capacity of the top level based upon NZSEE seismic assessment guidelines [11] and ASCE 41 [27]**

<b>Pier (Top Storey)</b>	$V_r$ ( $\alpha = 1.0$ ) (kN)	$V_r$ ( $\alpha = 0.5$ ) (kN)	$V_{tc}$ ( $\alpha = 1.0$ ) (kN)	$V_{tc}$ ( $\alpha = 0.5$ ) (kN)	$V_{dt}$ (kN)	$V_s$ (kN)	$V_{r,flanged}$ ( $\alpha = 1.0$ ) (kN)	$V_{r,flanged}$ ( $\alpha = 0.5$ ) (kN)
<b>North</b>	18	10	20	11	49	87	24	15
<b>Middle</b>	37	21	40	23	84	140	37	21
<b>South</b>	18	10	20	11	49	87	19	12
<b>Total</b>	<b>73</b>	<b>41</b>	<b>80</b>	<b>45</b>	<b>182</b>	<b>314</b>	<b>80</b>	<b>48</b>

A series of load applications and releases were applied by the excavator to simulate semi-cyclic loading. Eight loading cycles were applied to the structure in total, with the point load magnitude ranging between 20 kN and 55 kN. It is noted that there was significant difficulty in controlling the magnitude of individual cycles due to the coarseness of the excavator control system, which can be observed with the different loading rates for

each cycle summarised in Table 3. Loading was only applied in the south direction as the excavator was unable to pull the wall in the north direction or access the building from the south side.

**Table 3. Applied loads and loading rate on test building**

Load Cycle	Max Load (kN)	Average Loading Rate (kN/s)
1	28.2	3.6
2	20.6	9.0
3	53.6	6.3
4	55.0	8.2
5	45.1	8.0
6	55.2	7.9
7	19.9	16.5
8	45.8	13.8



(a) Schematic showing loading of N-W corner (b) Photograph of north elevation prior to load application

Figure 2. Excavator preparing to apply load for pushover testing

### 3.1 Instrumentation

The overall load deformation response was measured with a load cell fixed at the roof level at the point of load

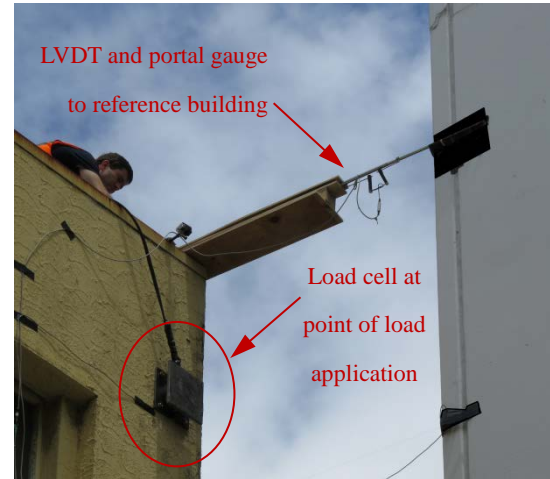
application. A steel plate attached to the load cell was used for the excavator to apply loads to the building without inducing damage to the load cell (see Figure 3c). Due to the anticipated rocking mechanism of the second storey piers, insignificant lateral load was expected to be transferred to the lower storey URM piers. This limited force transfer, limited site access, and tight time restraints resulted in only the second storey URM piers being heavily instrumented (see Figure 3a). Vertical deformations at the ends of each URM pier were measured to quantify pier uplift and rotation. The overall displacement of the building near to the point of load application was measured with an exterior LVDT mounted to the roof and by measuring displacements relative to the adjacent “reference” building (see Figure 3d).



(a) West-facing interior view of second storey test wall showing instrumentation. Push loading was applied to the North pier



(b) Installation of external instrumentation



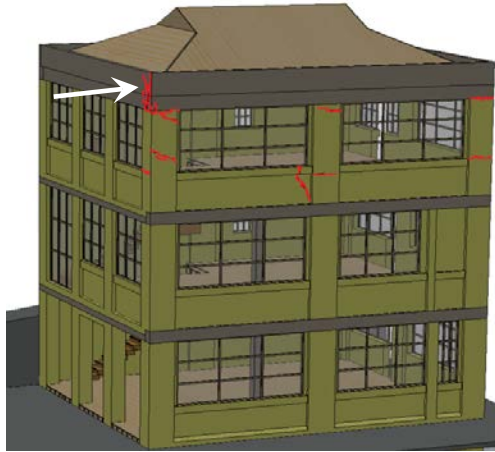
(c) Load cell with loading plate and LVDT mounted to adjacent reference building

Figure 3. Test instrumentation

## 4 OBSERVED DAMAGE AND BEHAVIOUR

### 4.1 Global Behaviour

Following the completion of eight loading cycles, horizontal cracking was observed at the top and bottom of each of the second storey URM piers (see Figure 4). The observed crack pattern was consistent with the predicted rocking response of the second storey URM piers. No cracking was observed on either the first or ground storeys, suggesting that as expected, the pier rocking limited the shear demands to the lower storeys. Multiple cracks radiating away and around the load cell were observed that appeared to be local effects of masonry damage at the point of load application.



(a) Observed crack damage (marked in red). Arrow indicates direction and location of load application

(b) Observed cracks widths (0.1 mm to 2.0 mm)

Figure 4. Observed cracking damage

The force-displacement behaviour of the west elevation is shown in Figure 5. Overall, the west elevation of the test building behaved in an elastic manner over the range of applied loading, with a consistent secant stiffness of approximately 16 kN/mm for each cycle. It should be noted that due to data acquisition complications, the hysteretic response of the initial (uncracked) stages of the test were not captured, including the initiation of cracking, and as such the force-displacement response shown in Figure 5 represents the cracked section behaviour for each cycle. The consistent secant stiffness observed is likely to be a result of all cycles representing the cracked section behaviour. Approximately 1 mm of residual displacement was observed during the portion of testing for which data acquisition was available. While the total residual displacement (defined with respect to the pre-test datum) was not measured, post-test observations of the top storey during crack mapping of the wall exterior indicated that any residual displacement was small. This small amount of residual displacement was attributed to local damage to the masonry in the area surrounding the applied load. The lack of significant residual displacement also suggested that there was no sliding of the concrete bond

beam at the top of the masonry piers and that the URM piers likely re-centred following load release.

A maximum load of 55.2 kN was obtained during testing (Table 3), as this was the largest load that could be generated by the excavator. As such, the full strength of the top storey was not able to be ascertained as was originally intended as part of the test programme, although the observed crack pattern and the small amount of non-linearity in the hysteretic response indicated that a pier rocking mechanism had initiated. The maximum load obtained during testing was approximately 75% of the estimated value for storey shear capacity using the NZSEE assessment guidelines [11] assuming full fixity at the top and bottom of each pier ( $\alpha = 1.0$ , Table 2) and 135% of the estimated value when assuming  $\alpha = 0.5$  (see Table 2). The lack of significant stiffness reduction in hysteretic response and failure to observe significant pier uplift due to rocking during testing is consistent with the assumption that the maximum test load was below the calculated rocking failure load of the top storey piers when assuming full top and bottom pier fixity, suggesting that the piers had remaining capacity and that the rocking mechanism was not fully developed. Whilst it is unclear what excavator force would have been required to fully develop the rocking failure mechanism, the reasoning described above suggests that the assumption of full fixity at both the top and bottom of the piers ( $\alpha = 1.0$ ) is appropriate for determining pier capacity for most assessment purposes. This approximation is useful for assessments in which such approximations often do not alter the assessment or remediation decisions of the whole building, as is the case for many buildings in practice, but is inappropriate if understanding the precise stiffness or capacity of a URM pier is of importance.

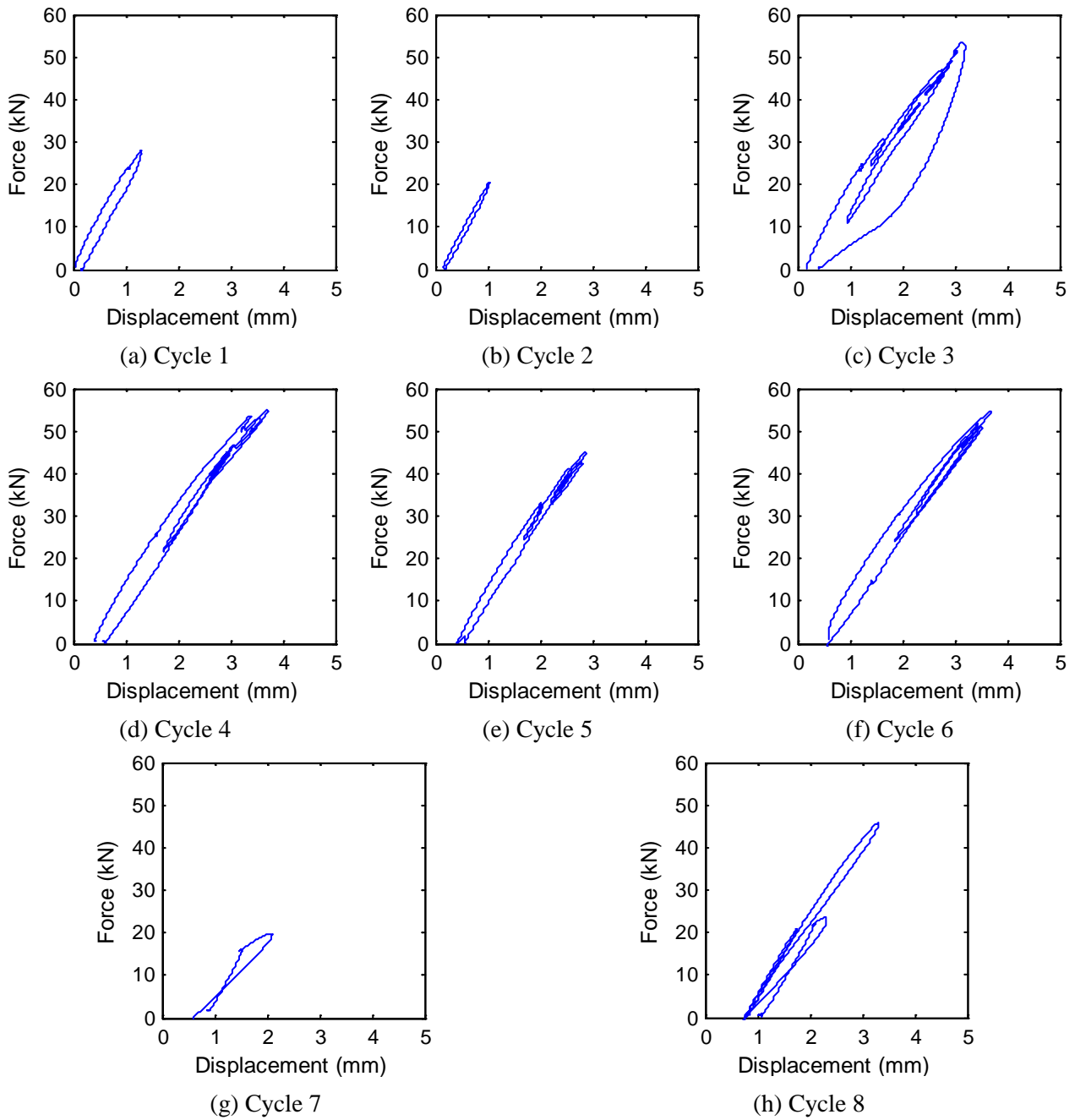


Figure 5. Force-displacement cycles of test wall at roof level. Note: displacement measured from exterior LVDT

#### 4.2 Pier Behaviour

The pier rotations with respect to applied loads are shown in Figure 6, in which the rotations at both the top and bottom of each pier are shown for the uni-directional loading (i.e. no “negative” reversed loading was applied because the excavator could only apply a push load to the building). Rotations at the top of the piers

were approximately four times greater than at the bottom, which is consistent with the large cracks observed at the pier tops after testing (see Figure 4a), suggesting that flexural deformation occurred in the piers, rather than pure rigid body rotation of the piers.

While the overall rotations for the north and middle piers were similar, the south pier experienced rotations of approximately twice the magnitude of the other piers at cycles with loading above 30 kN (see Figure 6). This increased rotation was most likely a result of the flange orientation at the north and south piers and the unidirectional loading (see Figure 3a for pier flange characteristics). Because the load was applied in only one direction, the north and south piers would be expected to have different lateral behaviour due to the opposite flange orientation between piers (see Figure 7). In the south pier, the flange was located on the compression face. When rocking initiated, the in-plane portion of the south pier cracked and the flange resisted the compression force. Because the flange was rocking out-of-plane, the moment of inertia and pier self-weight resisting the lateral load in the south pier was smaller than for the other two piers. Conversely, the north pier flange was located on the tension side of the section (see Figure 7). When cracking initiated through the flange, the north pier still had the majority of the in-plane portion to resist load, which had a much larger moment of inertia than the cracked section of the south pier. Also, the self-weight and roof load were located such that they acted to resist overturning and as a result worked to supplement the larger moment of inertia of the north pier to reduce the overall rotations. This discrepancy in stiffness between the North and South piers is consistent with the variation in strength between these two piers as predicted by the NZSEE assessment

guidelines for flanged rocking and shown in Table 2.

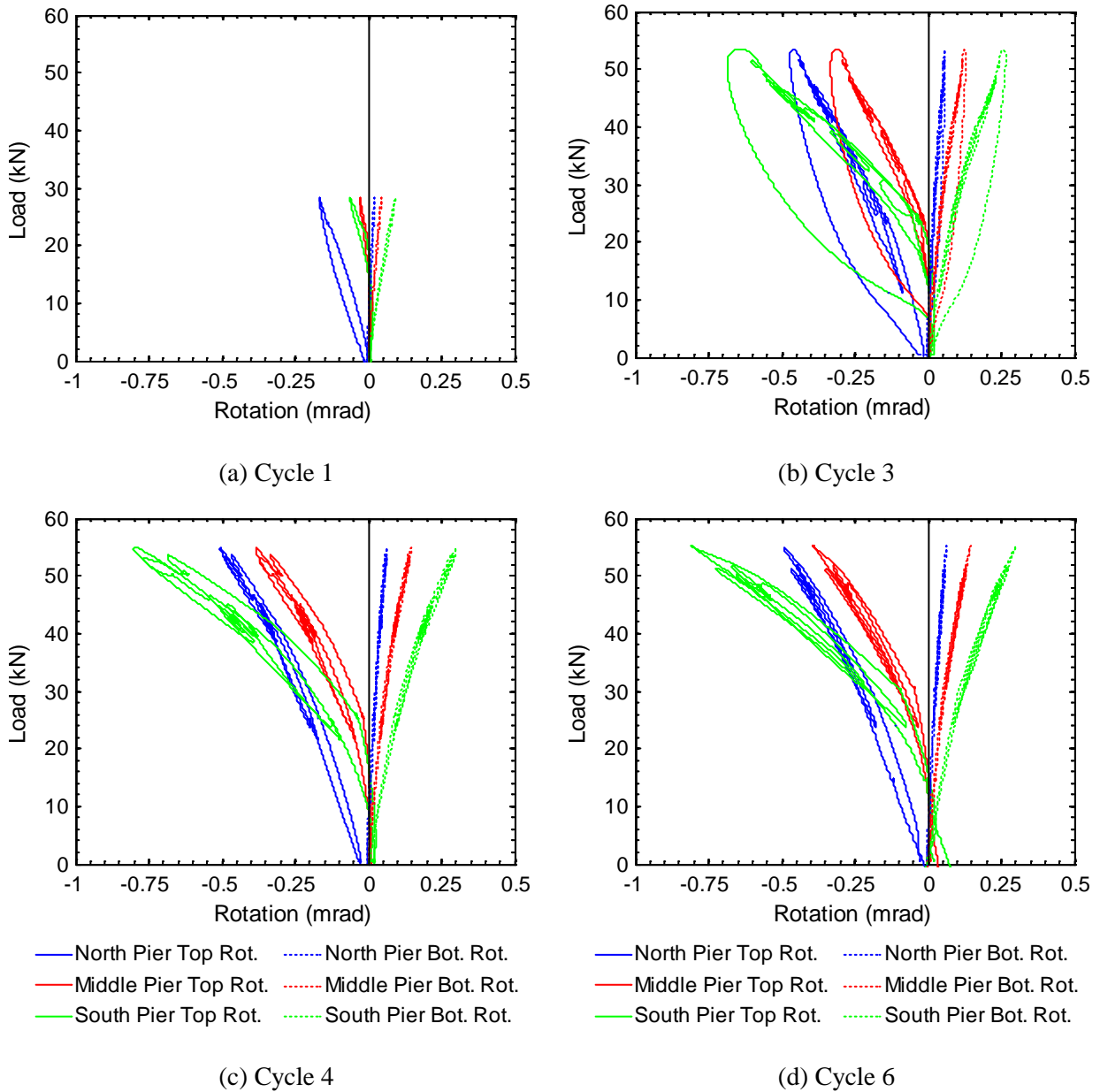
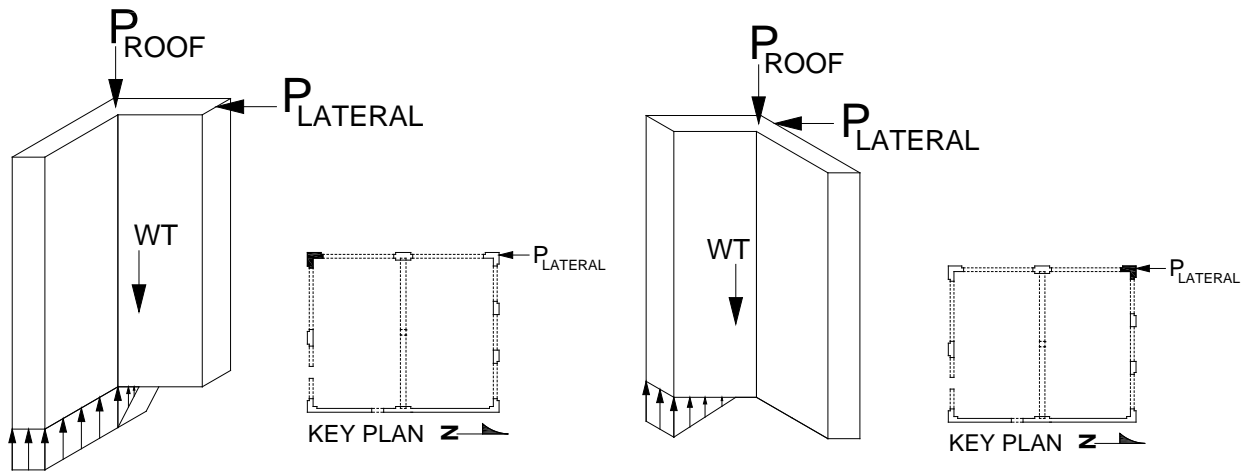


Figure 6. Selected experimentally measured pier rotation cycles of the test building at the second storey west façade



(a) Load distribution on South Pier

(b) Load distribution on North Pier

Figure 7. Corner pier load distribution. Pier location in test building highlighted in key plan.

## 5 FINITE ELEMENT (FE) MODELLING OF TEST BEHAVIOUR

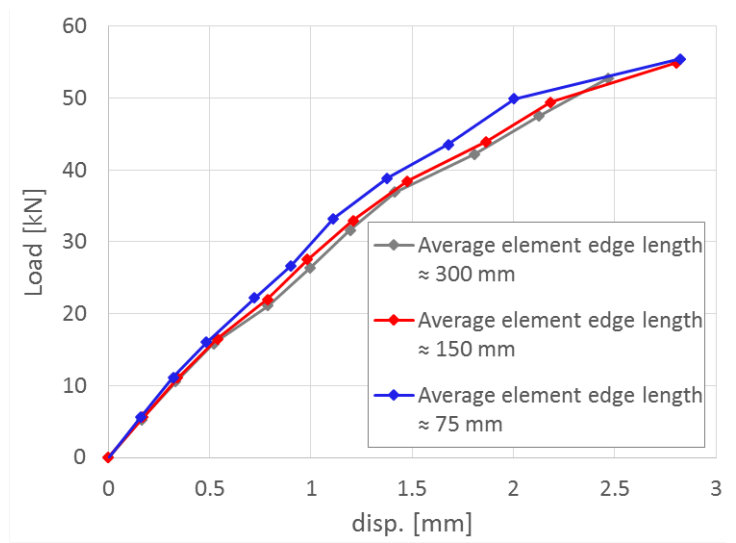
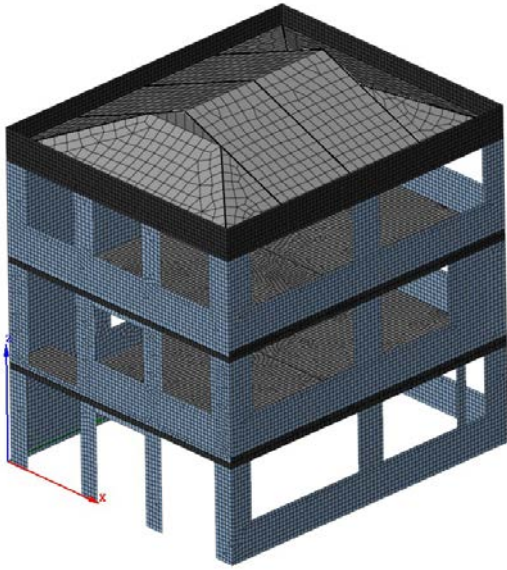
In order to investigate the behaviour of the test building when subjected to larger force and displacement demands and with more realistic boundary conditions and material properties, the building was modelled using the finite element (FE) software DIANA [29]. The model was generated based upon site assessed geometry and material properties and was calibrated using the force-displacement response observed during testing. A description of the model development and calibration process is presented in the following sections.

### 5.1 Model description

The FE strategy for the pushover analysis was based on the total strain smeared crack approach available in DIANA [29]. Masonry walls, timber diaphragms, concrete parapets, and concrete bond-beams were meshed by using curved shell elements with quadratic shape functions (8-node quadrilateral elements and 6-node triangular elements). One dimensional beam elements and truss elements were adopted for modelling the central support beams, the central columns, and the roof trusses. Based on onsite inspections, orthogonal

intersecting masonry walls were considered as “well-interconnected”, and to ensure appropriate representation of these connections, element “free edges” were removed at every wall-corner by making each corner-node common to both mesh sets. This assumption was adopted for all masonry-to-masonry, concrete-to-concrete and diaphragm-to-masonry interface surfaces.

The smeared crack approach is known to be mesh sensitive as the energy dissipated during the cracking process is dependent on the size of the finite elements. This dependency can be effectively mitigated by referring to a crack bandwidth as proposed by Bazant and Oh [30]. When specific input values for the crack bandwidth are absent, the default length for quadratic elements in DIANA is equal to the square root of the element area. In order to investigate the model sensitivity to element mesh size, a nonlinear pushover was performed on the model with three different mesh sizes for the nonlinear masonry and concrete elements (Figure 8). The crack bandwidth was determined as described by Bazant and Oh [30], and the maximum element size was limited by the geometry of the structural elements. Mesh quality was checked by referring to the utilities embedded in the software package. As can be seen in Figure 8b, the model had limited sensitivity to mesh size, with the same secant stiffness at 2.5 mm displacement and only slightly higher tangent stiffness when a mesh of 75 mm average element length was used. Given the limited sensitivity of the model to mesh size, a mesh of 150 mm was used for all subsequent analyses.



(a) Average masonry/concrete element size:  
150x150 mm<sup>2</sup> (quadrilateral)

(b) Capacity curve comparison of different model mesh sizes (loading scheme as per experimental pushover)

Figure 8. Sensitivity of the building model to the mesh size (nonlinear analysis with smeared cracking)

Material input parameters for concrete and masonry elements were taken in accordance with the material test data reported in Table 1. Linear softening and a nonlinear parabolic softening were adopted for concrete behaviour in tension and in compression respectively. Fracture energy values were determined as recommended by Model Code 90 [31]. An orthotropic linear elastic behaviour was attributed to the timber diaphragms with an equivalent shear stiffness equal to  $Gd = 180 \text{ kN/m}$ .

The linear tension softening response that was selected for the masonry was defined through the tensile fracture energy  $G_f$ , which is related to the tensile strength  $f_t$  (plane of failure perpendicular to the bed joints) via a ductility index in tension  $d_{u,t}$ . Initially  $f_t$  was assumed equal to the mean experimental value of the flexural bond strength ( $f'_{fb} = 0.34 \text{ MPa}$ ). This tensile strength resulted in a bi-linear pushover curve with cracked

behaviour initiating at a load level of approximately 40 kN and resulting in a reduction of stiffness to approximately 45%, which is contrary to experimental observations (Figure 9). Due to the variation in the experimental value of the flexural bond strength ( $CoV = 0.58$ ), sensitivity analyses on masonry tensile strength were performed. A reduction of the tensile strength value resulted in a smoother pushover response curve, with crack formation occurring as soon as the lateral load was applied. The lower bound value (mean value minus one standard deviation,  $f_{t,lower\ bound} = f'_{fb} - \sigma_{f'_{fb}}$ ) of  $f_{t,l} = 0.1\ MPa$  was considered a reasonable choice (Figure 9) as this selection corresponded to a crack pattern in the model that was compatible with the damage observed during the testing (Figure 10). Values of  $f_t$  smaller than 0.075 MPa lead to an excessively large amount of cracking when compared to field observations and shifted the pier failure mechanism from rocking to shear failure. For values of  $f_t$  larger than the mean of  $f'_{fb}$ , the model responded elastically up to the loading corresponding to the maximum experimentally applied force (Figure 9). It should be noted that the selected lower bound  $f_t$  value of 0.1 corresponds with the values suggested by Eurocode 6 [32] in which for masonry prisms where the mortar compressive strength is less than 5 MPa (cf 4.3 MPa as reported in Table 1), the characteristic values of flexural tensile strength range from 0.05 MPa to 0.10 MPa.

As mentioned previously, fracture energy in tension ( $G_t$ ) is a fundamental parameter in determining the numerical response, as it governs the tension softening: if  $G_t$  is reduced, the number of cracks increases and the overall stiffness diminishes. Experimental evidence available in literature [33 – 35] suggests that typical values of  $d_{u,t}$  can be assumed to be between approximately 0.01 mm and 0.05 mm (Lourenco [35]

recommends a value of 0.029 mm). For the present case study,  $d_{u,t} = 0.015$  was found to be the value that ensured the best agreement with the experimental behaviour.

A nonlinear parabolic softening was employed for the compressive behaviour, where the compressive fracture energy  $G_c$  was obtained by adopting a ductility index in compression  $d_{u,c} = 1.6 \text{ mm}$  as recommended by Lourenco [36]. Because of the low compression level in the area of the building affected by the lateral loading, the model response to the experimental pushover simulation showed no sensitivity to the variation of masonry compressive strength (range:  $f'_m \pm \sigma_{f'_m}$ ) or compressive fracture energy (range:  $d_{u,c} \pm 50\%d_{u,c}$ ). Poisson's ratio for masonry elements was assumed to be  $\nu = 0.25$ .

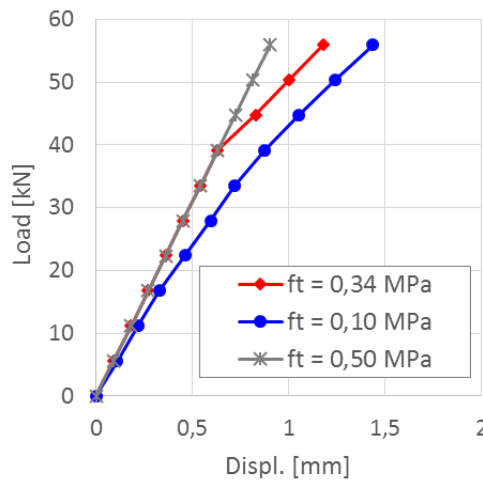


Figure 9. Pushover response with different masonry flexural tensile strengths

## 5.2 Model results and comparison to experimental response

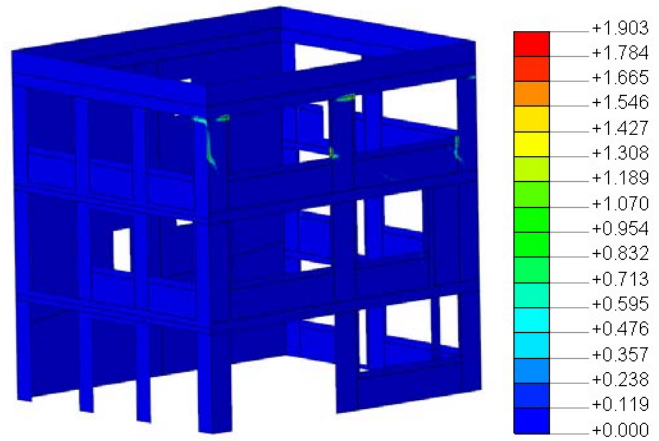
The FE model of the building was subjected to a point load at the northwest corner of the roof level to simulate the loading during experimental testing. As shown in Figure 10 the crack pattern obtained from the numerical model was compared to that observed from the tested building. Consistent with the experimental behaviour,

pier-rocking at the building top level (west) dominated the numerical response, with the formation of horizontal cracks at the top and at the bottom of the masonry panels. No cracking greater than 0.05 mm was observed elsewhere in the building.

While the numerically forecasted crack formation was consistent with that observed during testing, the pushover curves obtained from the finite element model were significantly stiffer than the curves measured during the tests as can be seen in Figure 11. Several variations of model formulations were attempted to investigate what behaviour was accounting for the stiffness increase. These models are summarised in Table 4. The model response was still significantly stiffer than the experimental even when a lower bound value for masonry modulus of elasticity ( $E_{m,lower\ bound} = E_{m,l} = E_m - \sigma_{E_m}$ ) was adopted (Figure 11, black curve). To investigate if the modelling of the diaphragm-to-masonry connections was artificially stiffening the building due to ineffective lateral connections, or whether minimal longitudinal sliding of the joists oriented parallel to the building west façade was allowed by the joist boundary conditions during the experimental pushover, a pushover test was also performed with the diaphragms removed from the model. As discernible from Figure 11, despite the assumption of ineffective diaphragms, the model stiffness was still not compatible with the experimental stiffness.



(a) experimentally observed cracks



(b) numerical results for last pushover cycle displacement (maximum crack width in mm)

Figure 10. Crack pattern from pushover testing on Rutland St Building

**Table 4. Model variations used in pushover modelling of test building**

Model	Elastic Modulus ( $E_m$ ) (MPa)	Diaphragm Connection to Walls	Secant Stiffness (kN/mm)	Ratio of Model Secant stiffness to Exp.
$E_m$	5630	Fixed	59.71	3.3
$E_{m,l}$	3441	Fixed	40.64	2.3
$E_{m\_ND}$	5360	No Connection	43.12	2.4
$E_{m,l\_ND}$	3441	No Connection	27.95	1.6

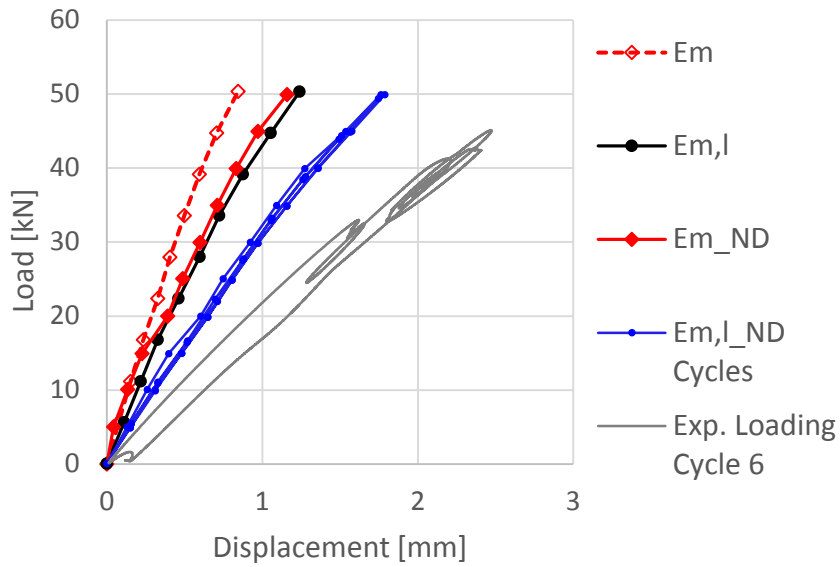


Figure 11. Pushover curve comparison between experimental roof deformations and load vs. numerical results for different model stiffnesses

As previously mentioned, the top storey of the building frame that was mobilised by the pushover testing was characterized by a low vertical stress level ( $\leq 0.2MPa$ ) that resulted in a large number of masonry bed joints being loaded in tension when lateral force was applied. Experimental data on masonry specimens loaded in tension by Rots [33] and Van der Pluijm [34] show that the elastic modulus of joints loaded in tension can be appreciably smaller than that of joints loaded in compression. Consequently, the elastic modulus in tension ( $E_T$ ) of the masonry walls located on the third level of the west façade was tentatively reduced to 65% of  $E_{m,l}$  in accordance with the findings from [33-34] to capture the more flexible flexural behaviour observed in the experiment. In order to do so, horizontal line interface elements were inserted between every element-row of the masonry mesh. The behaviour attributed to the interface elements was linear elastic in tension while rigid

in compression and shear. The tension stiffness of the line interface elements  $k_T$  (per unit of interface area) was determined according to Equation 1, by considering that the interface elements respond in series with the shell elements.

$$k_T = (E_T E_{m,l}) / [h(E_{m,l} - E_T)] \times (m/n) \quad (1)$$

where  $h$  is the average length of the shell elements,  $m$  is the number of interface lines in a mesh set and  $n$  is the number of element rows in a mesh set. The resulting capacity curves, which are given in Figure 12, showed an improved agreement with the experimental data.

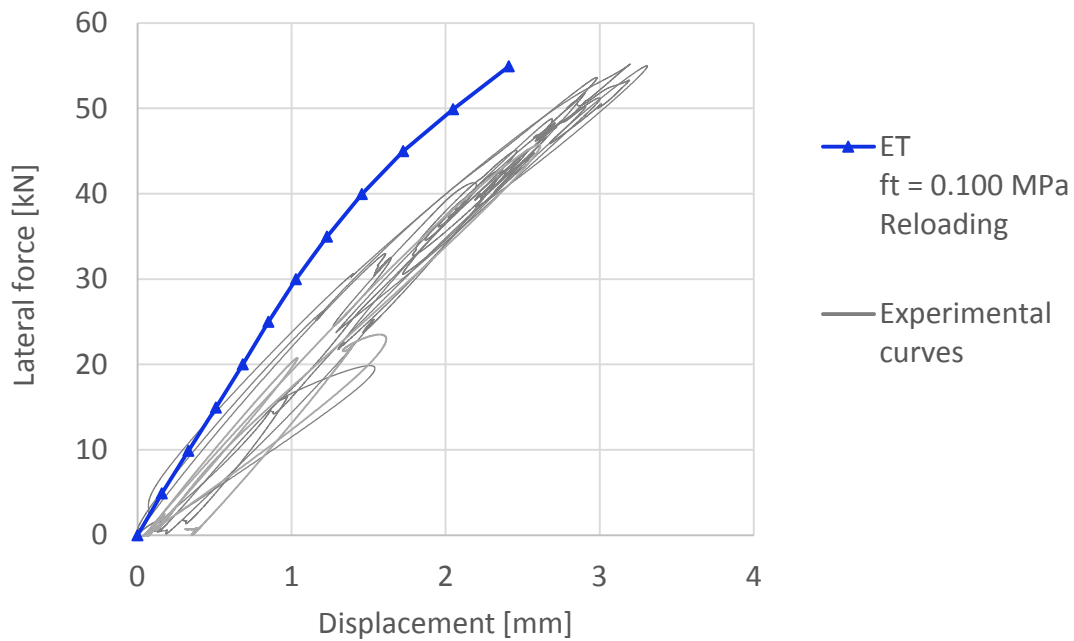


Figure 12. Pushover curve comparison between experimental results and numerical results with reduced masonry elastic modulus in tension at the third level

The lack of shear sliding failure mechanisms was checked by combining a multi-fixed smeared cracking approach with a Mohr-Coulomb plasticity criterion. No change in response was observed between the two

methods, as cracking occurred in the piers prior to the shear stress reaching the yield surface of the Mohr-Coulomb criterion.

Damage progression due to cycle repetitions was accounted for by adopting the secant unloading scheme in DIANA associated with the total strain smeared crack approach. Numerical cyclic repetitions resulted in limited stiffness deterioration (an example is reported in Figure 11: blue line), in accordance with the almost constant secant stiffness that was observed experimentally.

## **6 EVALUATION OF COMMON ASSESSMENT METHODS**

Following the calibration of the FE model with the experimental results, the FE model of the test building was used to investigate the response of the building to failure. The FE model of the entire building was subjected to a pushover analysis with mass proportional loading applied in the North-South direction. The response of the FE model was compared to two assessment techniques, which are commonly used by design engineers to assess the failure mechanism, the strength, and the deformation capacity of URM buildings. The first of these techniques utilized the equations provided in Section 8 of the NZSEE Seismic Assessment Guidelines [11] and in ASCE 41 [27], and the second technique involved a 2D macro-element (ME) model using the software package TREMURI [38]. The response of the alternative techniques was compared with the calibrated FE model using material properties matching the calibrated model as well as the mean, upper, and lower bound material properties presented in Table 1, and the consequence of these different modelling choices was investigated.

## 6.1 Pushover Response of the finite element (FE) model

Figure 13 shows the pushover curves obtained from the finite element model when subjected to increasing lateral loading. Mass proportional loading was applied in the North-South loading direction, and the Northwest corner of the roof was used as the control point to maintain consistency with the experimental testing. As expected, the adoption of the lower bound value for the masonry MoE (dashed black line in Figure 13) in lieu of the mean value (solid black line in Figure 13) decreased the overall stiffness, with a negligible effect on the maximum shear capacity, which was approximately 520 kN. In order to provide a more direct comparison to the NZSEE/ASCE assessment methods and macro element model, the FEM was run with the connections between orthogonal intersecting walls are ineffective, such behaviour is inherent in the formulation of both the NZSEE/ASCE and ME models. The response of the ineffective wall connection FE model permutations are shown in red in Figure 13, and as expected, the lack of effective connection between the walls resulted in a further stiffness reduction.

Analysis of the crack pattern evolution showed that damage mainly occurred on the West façade, with the onset of pier rocking mechanisms at all storey levels, diffused cracking in the spandrels at the second level (Figure 14a), followed by diagonal shear failure of the piers at the ground level (Figure 14b). In conjunction with shear failure developing in the piers on the West façade, diffused in-plane cracking simultaneously started to develop on the other building façades (Figure 15). It should be noted that the crack width maps shown in Figure 14b and Figure 15 are at different scales.

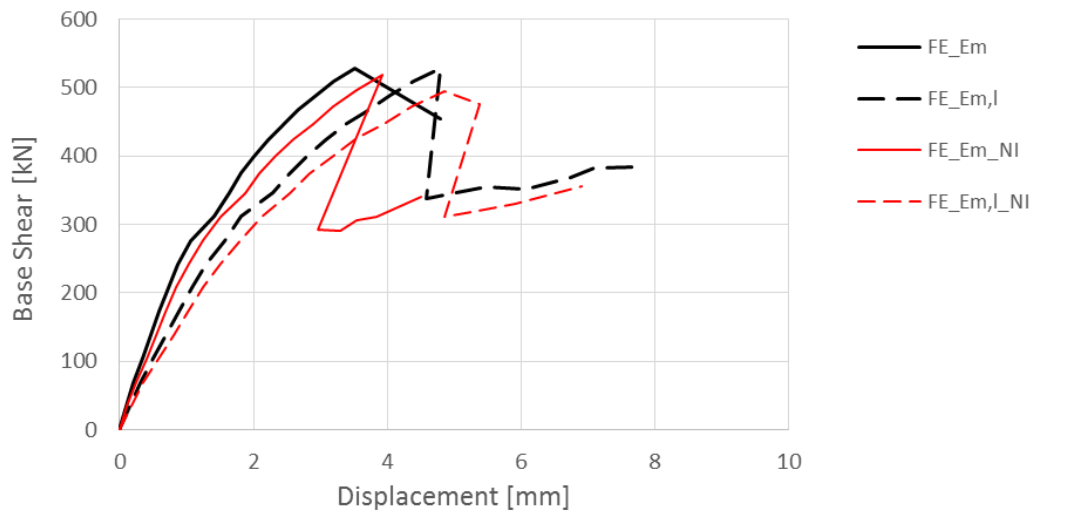


Figure 13 Building capacity curves of the finite element (FE) model for mass proportional loading in the North-South direction. (The subscripts Em = mean modulus of elasticity of masonry, Em,I = lower bound modulus of elasticity of masonry, and NI = ineffective connection between orthogonal walls).

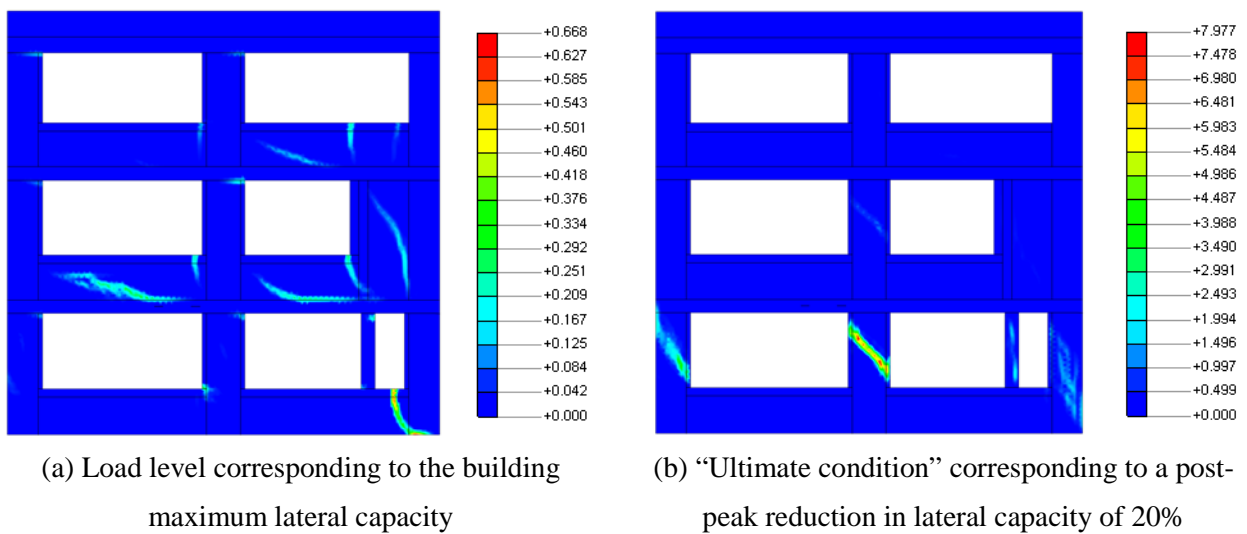


Figure 14 FE-model damage pattern evolution on West façade (scale shows principal crack width [mm]).

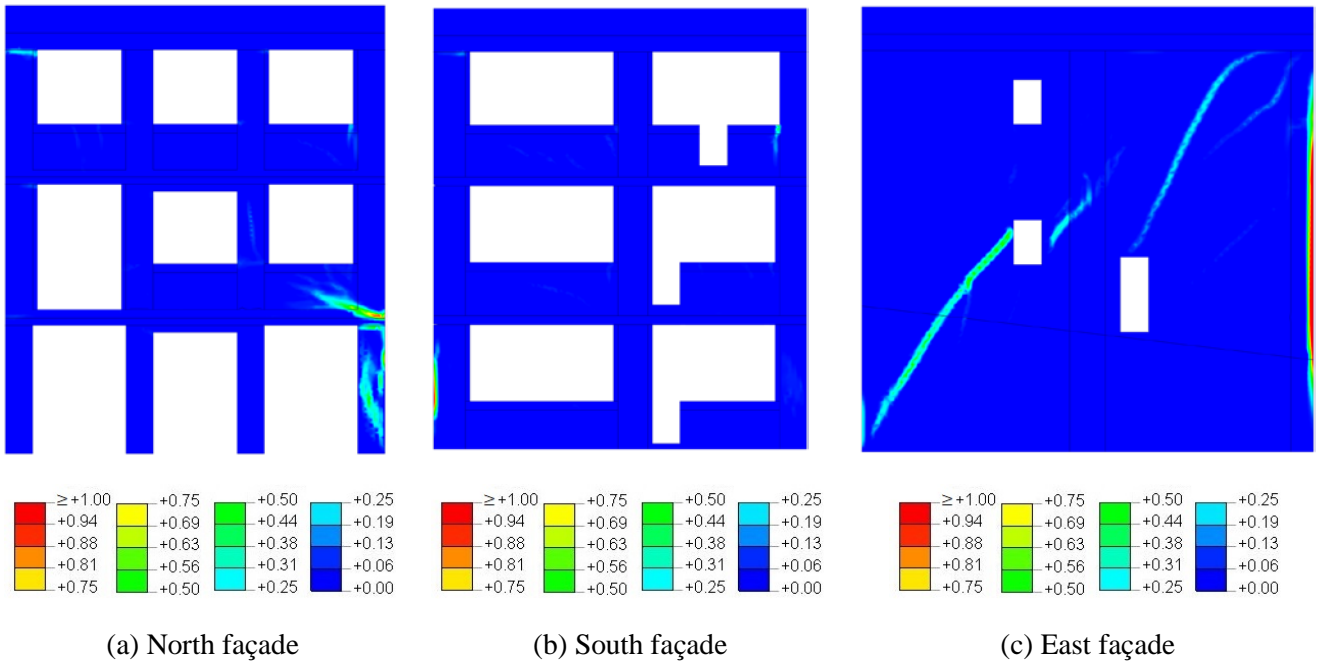


Figure 15 FE-model damage patterns on South and East facades at ultimate condition (scale shows principal crack width [mm])

## 6.2 Strength capacity based upon NZSEE and ASCE 41 guidelines

The lateral load capacity of the building in the North-South direction was predicted using the strength assessment recommendations in NZSEE [11] and ASCE 41 [27]. Material properties determined from site investigation and laboratory testing were assumed in the predictive models, including the density of masonry ( $\rho_m$ ) being  $18 \text{ kN/m}^3$ , the cohesion of the bed joints ( $c$ ) being  $0.33 \text{ MPa}$ , and the masonry compressive strength ( $f'_m$ ) being  $6.3 \text{ MPa}$ . Additionally, the masonry coefficient of friction ( $\mu_f$ ) was assumed to be  $0.3$  [12, 21].

The West façade capacity was calculated on a storey by storey basis, with all piers in the bottom two storeys assumed to have fixed boundary conditions at the top and bottom, with the top storey piers having capacities determined for both fixed and free pier top conditions ( $\alpha=1.0$  and  $\alpha=0.5$ , respectively). It was determined

that the piers at each storey would be subject to rocking failure followed by toe crushing. The East façade capacity was calculated based upon the entire height of the East wall from ground level to roof, ignoring the contribution of the basement, and assuming no perforations as is common engineering practice when the openings are of relatively small size and number as were those in the test building. The East façade was assumed to be a fixed-free cantilever with the ability to rotate at the wall top. It was assumed that for in-plane behaviour an equivalent horizontal force was applied at  $2/3$  the height of the East façade. The capacities for each storey and façade are summarised in Table 5.

To estimate the base shear at first failure of the lateral resisting system, the seismic demand at each storey and for each façade was determined based upon mass proportional loading of each line of action, which was determined based upon tributary area due to the flexible diaphragms present in the test building. Because the top storey of the West façade had the smallest seismic mass, the demands on the other storeys of the West façade and the East façade were normalised with respect to this mass. Similarly, the capacities of each storey were normalised with respect to the top storey of the West façade and it was established that the demand to capacity ratio of the top storey of the West façade was smaller than for the other resisting elements and as such the top storey of the West façade would fail first. To estimate the base shear at this initial failure, the demands for each storey were summed for both the case in which the top storey West piers were fixed at both top and bottom ( $\alpha=1.0$ ) as well as when assuming that fixity was only at the pier base ( $\alpha=0.5$ ). These two cases can be assumed to be the upper and lower bound base shears for the building at the initiation of failure of the top

storey and are equivalent to 561 kN for the piers with fixed-fixed conditions and 315 kN for the case of fixed-free conditions.

**Table 5. Predicted pier and wall capacity and demand based upon NZSEE seismic assessment guidelines [11] and ASCE 41 [27]**

	Seismic Mass (Tonnes)	Ratio to Mass of Top Storey W. Façade	Capacity (kN)	Ratio to Capacity of Top Storey W. Façade	Demand at Top Storey W. Façade Failure (kN)
<b>West Façade Top Storey</b>	23.8	1.00	73 (if $\alpha=1.0$ ) 41 (if $\alpha=0.5$ )	1.00	73 (if $\alpha=1.0$ ) 41 (if $\alpha=0.5$ )
<b>West Façade 2nd Storey</b>	31.5	1.32	255 ( $\alpha=1.0$ )	3.49	97
<b>West Façade 1st Storey</b>	34.4	1.44	286 ( $\alpha=1.0$ )	3.92	105
<b>East Façade (entire wall)</b>	93.2	3.91	491 ( $\alpha=0.5$ )	6.73	286
<b>Base Shear at Failure of Top Storey West Façade (<math>\alpha=1.0</math> for top storey):</b>					<b>561 kN</b>
<b>Base Shear at Failure of Top Storey West Façade (<math>\alpha=0.5</math> for top storey):</b>					<b>315 kN</b>

### 6.3 Pushover response of the macro-element (ME) model

The seismic response prediction obtained from the finite element model using DIANA software was also compared to that determined by adopting a macro-element approach where masonry piers and spandrels are modelled by single elements intersecting each other at rigid nodes [37] using TREMURI software [38]. The ME model (including geometric simplifications such as uniform wall thickness) is shown in Figure 16. The macro-element masonry panels were characterized by a bilinear behaviour consisting of a linear elastic phase followed by perfect plasticity. The plastic threshold was assumed to be reached when the one of the following failure modes was activated: rocking, shear sliding, or shear cracking. Rocking capacity ( $M_{rd}$ ,  $V_{rd}$ ) was

determined assuming that the masonry had zero tensile strength and experienced uniform stress distribution in compression using Equation 2. The coefficient  $\alpha$  depends on fixity conditions at the pier ends (e.g.  $\alpha=0.5$  when the pier is fixed at one end,  $\alpha=1$  when the pier is fixed at both ends). Shear sliding capacity ( $V_s$ ) was assumed to be reached when the shear stress in the ME model reached the boundary of a Mohr-Coulomb failure surface assuming a friction coefficient of 0.4. Diagonal shear capacity ( $V_{dt}$ ) was predicted by adopting the Turnšek and Cačovic [39] criterion as formulated in Eq. 3:

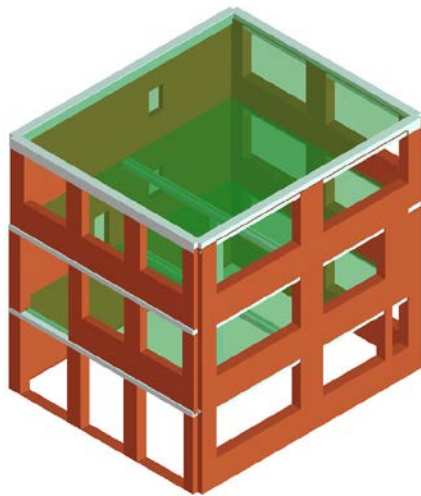
$$M_{rd} = \left( \frac{L^2 t \sigma_0}{2} \right) \times \left( 1 - \frac{\sigma_0}{0.85 f_m} \right), \quad V_{rd} = (2\alpha M_{rd})/H, \quad 0.5 \leq \alpha \leq 1 \quad (2)$$

$$V_{dt} = (L t f_{t,cr}/b) \times (1 + \sigma_0/f_{t,cr})^{0.5} = (L t 1.5\tau_0/b) \times (1 + \sigma_0/1.5\tau_0)^{0.5} \quad (3)$$

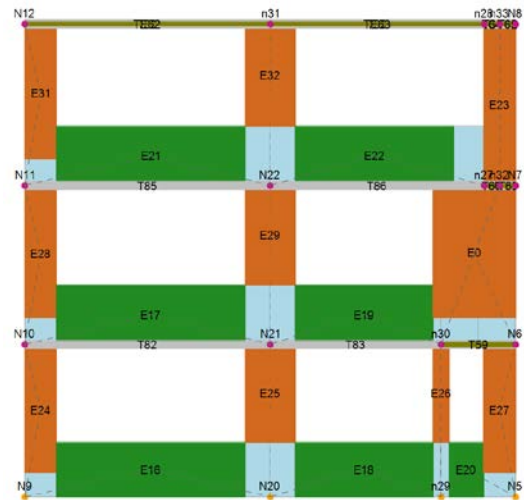
where  $L$  is the wall length,  $t$  is the wall thickness,  $\sigma_0$  is the average compressive stress,  $f_{t,cr}$  is the masonry tensile strength associated with the shear cracking mechanism,  $\tau_0$  is masonry shear strength under zero axial loading and  $b$  is a coefficient that depends on the wall aspect ratio. Equations 2 and 3 do not include safety factors.

The deformation of the macro-elements was limited by maximum acceptable inter-storey drift values, which were taken in accordance with NTC [40]. A life safety drift limit of 0.4% was adopted for shear failure, consistent with suggestions in ASCE [27] and NZSEE [11] and as validated by research studies such as Magenes and Calvi [1] and Priestley et al. [41]. The 0.6% drift limit value was selected for rocking failure, in accordance with NTC [40]. This rocking drift limit appears to be conservative if compared to the 1% drift value recommended by Magenes and Calvi [1]. Conversely, in the case of slender piers where the wall height is approximately twice the wall length, the 0.6% drift limit corresponds with the limiting value proposed by

NZSEE [11], which is  $0.3\% \times (\text{wall height} / \text{wall length})$ .



(a) overview of building model



(b) mesh details of West façade (green = spandrel element; brown = pier element; light blue = rigid node; grey = concrete beam element)

Figure 16 Macro-element model overview and West façade model components

Multiple model formulations were investigated to determine the change in response of the model to different shear failure criterion, masonry stiffness, masonry tensile strength, and diaphragm type, and how these parameters altered the response with respect to the calibrated FE model pushover response. These different model permutations are summarised in Table 6. Shown in Figure 17 are the resulting capacity curves obtained from the pushover analysis performed with the ME model. Irrespective of the shear failure criterion or the masonry MoE value selected, the model showed a maximum capacity of approximately 350 kN (33% smaller than the capacity from the FE model), with failure characterized by rocking of the piers at the ground level of the West façade (Figure 18). Because of the spandrel geometry and the presence of the concrete

ringbeams, the maximum shear force sustained by the West façade ( $\approx 150$  kN) corresponded to the sum of the  $V_{rd}$  shear capacities of the piers determined from the shear-type building model assumption ( $\alpha = 1$ , Eq. 2). As already mentioned, unlike the FE model (Figure 19a), the ME model showed no damage in the other building façades, with the elements remaining well within their elastic phase throughout the entire analysis (Figure 19b). When the rigid diaphragm option was selected (Figure 19c) a significant increase in the building capacity was observed (Figure 17), with more load being transferred to the East façade and also the engagement of the rocking capacity of the piers on the North façade (Figure 19c, compare also Figure 19c with Figure 19a). The resulting capacity appears to be compatible with the capacity level exhibited by the FE model. This disparate behaviour shown by the two models was partially attributed to the stiffening effect on the diaphragms produced by the connections at the façade corners between concrete elements that ran perpendicular to each other in the FE model. When the concrete elements were prevented from transferring out-of-plane bending moments to the adjacent perpendicular elements, the FE response became closer to that of the ME model (see curve labelled as *FE\_Em\_NIC* in Figure 17).

The final ME model variation utilized a  $f_{t,cr}$  value equal to the value adopted for  $f_t$  in the FE modelling (i.e. 0.1 MPa). The initial stiffness and the base shear capacity of this model remained unaltered (see the curve labelled as *ME\_TkC\_Em\_RD\_ft = 0.1* in Figure 17) but the model experienced a change in failure mode. The new failure had the spandrels exceeding their plastic threshold, and the central pier at the ground level of West façade failing in shear (Figure 18b), similarly to what was observed from the FE model (Figure 14).

**Table 6. Model variations used in ME model formulation**

Model	Shear Failure Criterion	Elastic Modulus ( $E_m$ ) (MPa)	Diaphragm Type	Masonry Tensile Strength (MPa)
ME_MhC_Em	Mohr-Coulomb	5630	Flexible	-
ME_MhC_Em,l	Mohr-Coulomb	3441	Flexible	-
ME_MhC_Em_RD	Mohr-Coulomb	5630	Rigid	-
ME_MhC_Em,l_RD	Mohr-Coulomb	3441	Rigid	-
ME_TkC_Em	Turnšek & Cačovic	5630	Flexible	0.66
ME_TkC_Em,l	Turnšek & Cačovic	3441	Flexible	0.66
ME_TkC_Em_RD	Turnšek & Cačovic	5630	Rigid	0.66
ME_TkC_Em,l_RD	Turnšek & Cačovic	3441	Rigid	0.66
ME_TkC_Em_RD_ft=1.0	Turnšek & Cačovic	5630	Rigid	0.1

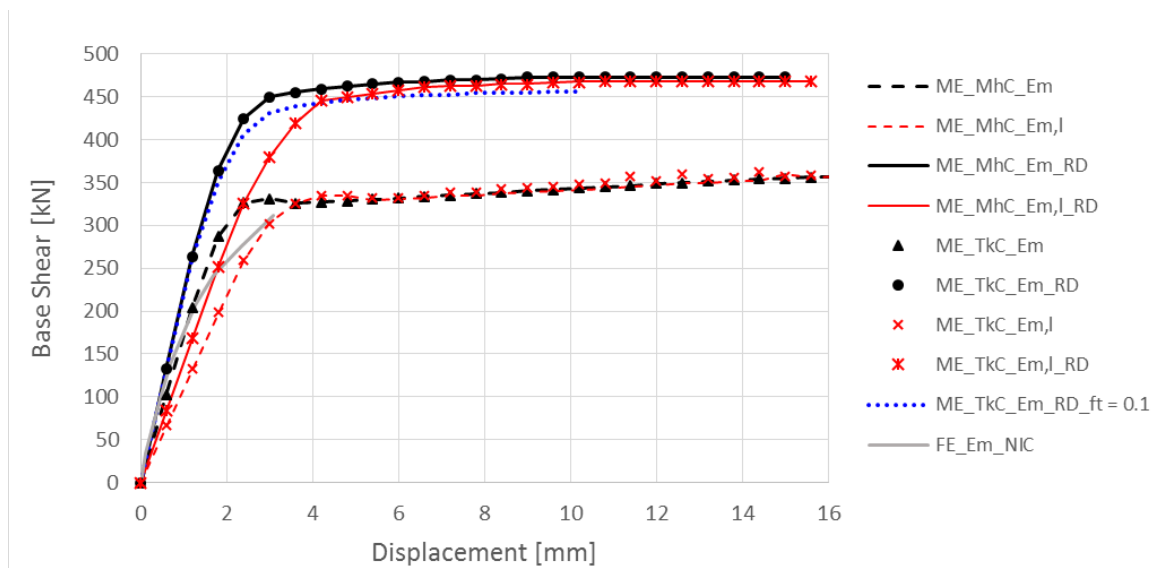
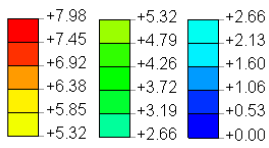
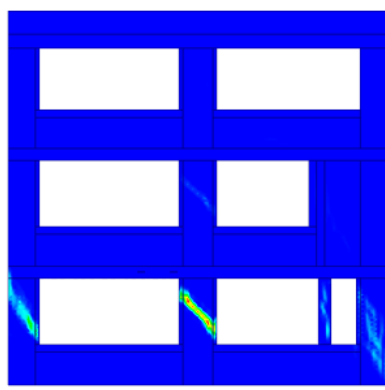
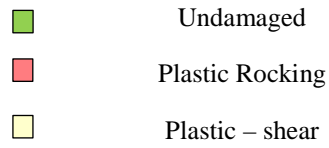
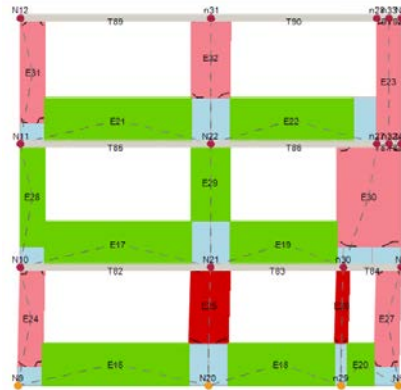


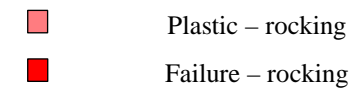
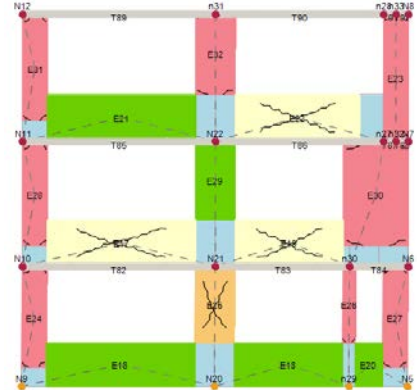
Figure 17 Macro-element (ME) model. Building capacity curves – North-South loading direction, load proportional to mass distribution (MhC = Mohr-Coulomb shear failure criterion, TkC = Turnšek & Cačovic [38] shear failure criterion, RD = rigid diaphragms, NIC = ineffective connection between orthogonal intersecting elements including concrete parapets and ring beams).



(a) FE model at ultimate capacity crack width [mm]

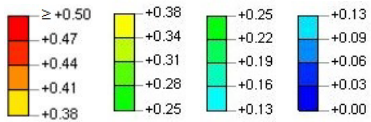
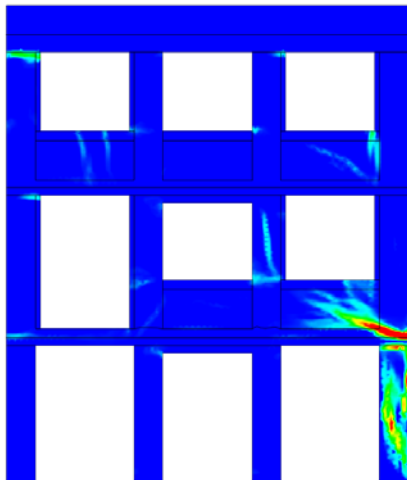


(b) Mohr-Coulomb and Turnšek & Cačovic shear failure criteria ( $f_{t,cr} = 1.5 \times \tau_0$ )

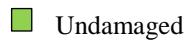


(c) Turnšek & Cačovic shear failure criterion ( $f_{t,cr} = f_t = 0.1 \text{ MPa}$ )

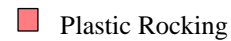
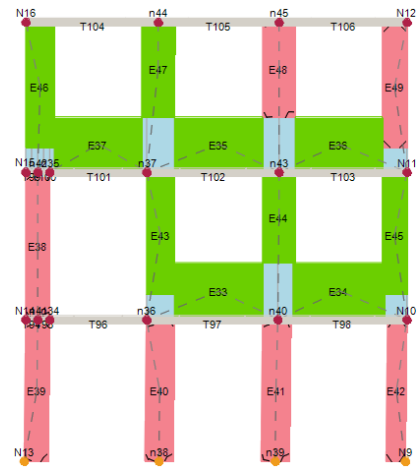
Figure 18 Damage pattern on West façade (perpendicular to the loading direction)



(a) FE model crack width [mm]



(b) ME model



(c) ME model (rigid diaphragms)

Figure 19 Damage pattern on North façade (perpendicular to the loading direction)

## 6.4 Response comparison

To investigate the ability of the simplified NZSEE/ASCE method and the ME modelling approach to replicate the behaviour from the calibrated FE model, the response curves provided by the three predictive modelling strategies are compared in Figure 20. Note that the ME modelling approach disregards bond connection between orthogonal walls (i.e., building corners). Furthermore, the ME modelling approach disregards the out-of-plane strength/stiffness of the walls. Hence, for a direct comparison to the ME predictive results, additional FE response curves were added to Figure 20. FE curves with the NI suffix represent models without an effective connection between orthogonal elements. FE curves with the additional IPW suffix represent models derived by neglecting the strength contribution from the façades perpendicular to the loading direction. As can be observed in Figure 20, the ME and the modified FE models predicted almost identical stiffness and similar capacity (difference < 10%), with failure modes consistent between the two models (see for example Figure 18 and Figure 19).

The main sensitivity of both the FE and ME models was found to be the selection of modulus of elasticity of masonry ( $E_m$ ). The use of a lower bound value of  $E_m$  was found to result in an approximately 33% reduction in stiffness from when the mean  $E_m$ , while the variation in the diaphragm stiffness or the connection between orthogonal walls only resulted in a 14% reduction in stiffness when compared to the baseline FE model. The use of a rigid diaphragm in the ME models was necessary to achieve similar capacity predictions to the FE model in order to enforce load sharing between each façade. It is assumed that this artificial diaphragm rigidity works well for a building of this size because the spans are relatively small and the building is quite

regular. Additionally, it is acknowledged that the out-of-plane wall strength and rigid connection between orthogonal walls also contributed to the artificial diaphragm rigidity reproducing the response of the FE model. It should be noted that given the approximate 150% increase in base shear capacity that the rigid diaphragm ME approach gives, it should be used with caution, as the present study is not extensive enough to provide detail as to the appropriate scenarios in which this approximation is appropriate. It is also noted that the drift limit values adopted for the macro-elements (0.4% for shear and 0.6% for rocking) resulted in the displacement capacity of the ME model being significantly larger than that observed from the FE model, even when failure was governed by shear.

The base shear at failure of the top storey of the West façade as predicted by the NZSEE [11] and ASCE 41 [27] seismic assessment guidelines, predicted a base shear of 561 kN when the top storey piers were assumed to be fixed at both the top and bottom ( $\alpha=1.0$ ), which over-estimated the FE model by approximately 8%. If the top storey piers were assumed to be free to rotate at the top ( $\alpha=0.5$ ), then the predicted base shear at the top storey failure was 314 kN. This value corresponds with the first appreciable stiffness reduction in the capacity curves of both the FE and ME models as well as the capacity of the ME models when the rigid diaphragm constraint is not induced ( $ME\_TkC\_Em/ME\_MhC/Em$ ). The sensitivity of the base shear capacity calculated based upon the NZSEE/ASCE 41 method occurs due to the significant strength discrepancies between the top storey piers of the West façade and the other resisting elements in the North-South direction of the building, resulting in the building capacity at first failure being controlled only by the

top storey of the West façade. As such, the calculated building capacity is highly sensitive to the boundary condition at the top of the piers and highlights that the binary choices of fixed or free pier tops may not be appropriate for some conditions. Furthermore, it is noted in the NZSEE guidelines [11] that when the axial load on the piers is high and the boundary conditions at the pier tops and bottoms are fixed-fixed, the equations for predicting the rocking capacity ( $V_r$ ) tend to over-predict rocking strength. It is unclear if the axial load applied to the top piers was high enough to account for such an effect.

Overall, it appears that a conservative approach for the assessment of the in-plane capacity of an URM frame-type building would be to assess either using the existing NZSEE/ASCE 41 assessment guidelines assuming mean values for masonry strength and stiffness and fixed-free pier boundary conditions at the top storey or to utilize 2D ME modelling of isolated facades with reduced drift limits.

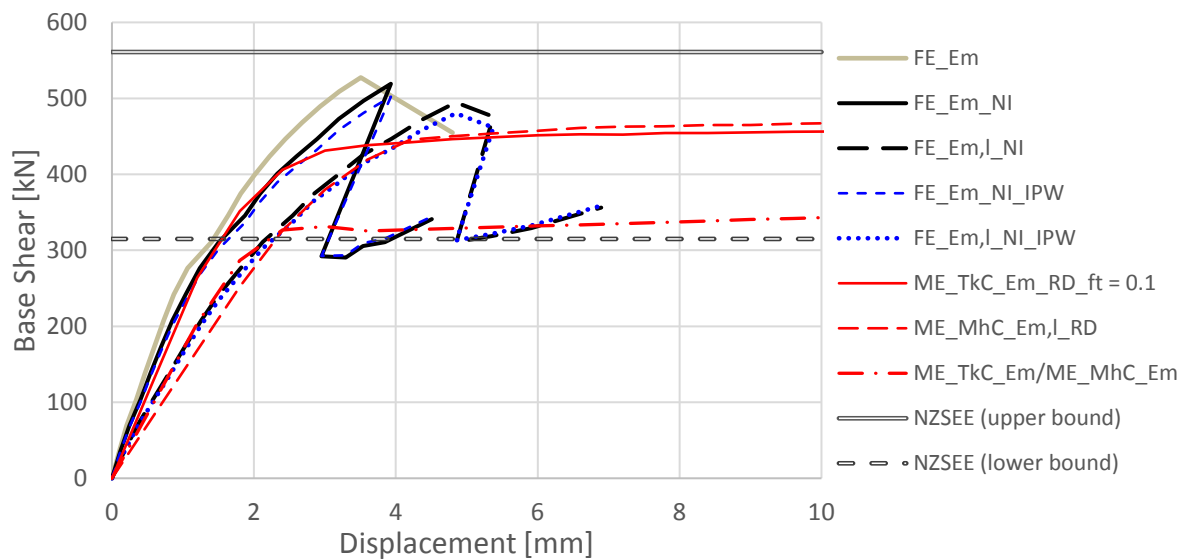


Figure 20 Capacity curve comparison (IPW = capacity contribution from the out-of-plane loaded wall is neglected).

## 7 CONCLUSIONS

Full-scale pushover testing of an existing vintage 3-storey URM building was successfully performed in order to help calibrate variables for the further development of seismic assessment tools. The observed crack pattern was consistent with the predicted rocking response of the second storey URM piers of the subject building. No cracking was observed on either the first or ground storeys, suggesting that pier rocking limited force transfer to the lower storeys. The RC bond beams appeared to provide adequate load transfer for load distribution among URM piers, and no sliding was anticipated nor observed during loading. During the experimental testing it was observed that the west wall of the test building behaved in an essentially elastic manner, with a consistent secant stiffness of approximately 16 kN/mm for each cycle.

Finite element modelling was conducted in order to represent the response observed during experimental testing. The following conclusions were made from the modelling study:

- The model was able to replicate the experimental failure mode, but the use of average and lower bound properties for the elastic modulus of masonry over-predicted the stiffness of the model.
- To match the experimental stiffness, the masonry elastic modulus was reduced when the elements acted in tension. This reduction in tension stiffness was consistent with the findings from previous small scale specimen testing [34-35].

Once the model response corresponded to the experimental results, the calibrated model was subjected to a pushover analysis and used to benchmark the ability for simplified assessment guidelines and macro-

element models to identify the failure mode and capacity of the test building response. It was found that:

- There was agreement between all methods on the identified rocking failure mode, as was expected due to this failure mode being predominately controlled by axial load and geometry, which were well constrained for each model.
- The macro-element model significantly under-predicted the capacity of the FE model unless a rigid diaphragm was assumed. The rigid diaphragm constraint was likely necessary to enforce connection between orthogonal walls which were not accounted for in the original macro-element model formulation, rather than to specifically elevate the diaphragm stiffness.
- The seismic assessment guidelines based on NZSEE and ASCE 41 [11, 27] also predicted rocking failure, but the base shear at first failure was very sensitive to the assumed boundary condition (free or fixed) at the top of the top storey piers.

From this study, the use of NZSEE and ASCE 41 assessment guidelines and 2D macro-element models of individual facades with reduced drift limits applied to the macro-element models was found to give a lower bound lateral load resisting capacity of the building and as such are deemed as appropriate assessment techniques for practicing engineers.

## **8 ACKNOWLEDGEMENTS**

The authors are grateful for the in-kind donations provided by DND Development Ltd. (owners of the building),

Peter Ward of Ward Group (demolition contractor in charge of the site), Racquel Lewis of Titivate Ltd, and Luke Austin of LADRA. Megan McNichols, Serguei Khairov, Yuri Dizhur, Jerome Quenneville, Ronald Gultom, Marat Khassenov, Laura Putri, and Royce Chin assisted with documenting building geometry and mobilising test equipment. Royce Chin, Mark Byrami, and Ross Reichardt assisted with materials testing. Financial support for this project was provided in part by the New Zealand Earthquake Commission (EQC). This project was partially supported by QuakeCoRE, a New Zealand Tertiary Education Commission-funded Centre. This is QuakeCoRE publication number 0184.

## 9 REFERENCES

- [1] Magenes, G. and Calvi, G.M. “In-plane seismic response of brick masonry walls.” *Earthquake Engineering and Structural Dynamics*. 1997; 26(11): 1091-1112, doi: 10.1002/(SICI)1096-9845(199711)26:11.
- [2] Russell, A. “Characterisation and Seismic Assessment of Unreinforced Masonry Buildings.” Department of Civil and Environmental Engineering Auckland, University of Auckland. PhD, 2010.
- [3] Knox, C. Assessment of perforated unreinforced masonry walls responding in-plane. Doctoral Dissertation, The University of Auckland, Auckland, New Zealand; 2012, <https://researchspace.auckland.ac.nz/handle/2292/19422>.
- [4] Dizhur, D. and Ingham, J. “Diagonal tension strength of vintage unreinforced clay brick masonry wall panels.” *Construction and Building Materials*. 2013; 43(0):418-427.
- [5] Parisi, F., Lignola, G.P., Augenti, N., Prota, A., and Manfredi, G. “Rocking response assessment of in-plane laterally-loaded masonry walls with openings.” *Engineering Structures*, 2013;56: 1234-1248, doi: <http://dx.doi.org/10.1016/j.engstruct.2013.06.041>
- [6] Moon, F. L., T. Yi, R. T. Leon and L. F. Kahn. “Testing of a Full-Scale Unreinforced Masonry Building Following Seismic Strengthening.” *Journal of Structural Engineering* 2007; 133(9): 1215-1226, doi: [http://dx.doi.org/10.1061/\(ASCE\)0733-9445\(2007\)133:9\(1215\)](http://dx.doi.org/10.1061/(ASCE)0733-9445(2007)133:9(1215))
- [7] Aldemir, A., Binici, B., Canbay, E. and Yakut, A. “Lateral Load testing of an existing two story masonry building up to near collapse,” *Bulletin of Earthquake Engineering*, 2015; doi:10.1007/s10518-015-9821-3
- [8] Russell, A. and Ingham, J. “Prevalence of New Zealand’s unreinforced masonry buildings.” *Bulletin of the New Zealand Society for Earthquake Engineering*, 2010; 43(3):182-201, [http://www.nzsee.org.nz/db/Bulletin/Archive/43\(3\)0182.pdf](http://www.nzsee.org.nz/db/Bulletin/Archive/43(3)0182.pdf).
- [9] Walsh, K., Dizhur, D., Almesfer, N, Cummiskey, P., Cousins, J., Derakhshan, H., Griffith, M., and Ingham, J. “Geometric Characterization and out-of-plane seismic stability of low-rise unreinforced brick masonry buildings in Auckland, New Zealand.” *Bulletin of the New Zealand Society for Earthquake Engineering*. 2014; 47(2):139–156.
- [10] Kaushik, H.B., Rai, D. C., and Jain, S.K. “Stress-Strain Characteristics of Clay Brick Masonry under Uniaxial Compression.” *Journal of Materials in Civil Engineering*. 2007; 19(9):728-739
- [11] NZSEE (New Zealand Society for Earthquake Engineering). Assessment and Improvement of the Structural Performance of Buildings in Earthquakes, Recommendations of a NZSEE Project Technical Group. Incorporated Corrigenda No. 4, Section 10, Seismic Assessment of Unreinforced Masonry Buildings, New Zealand Society for Earthquake Engineering, Wellington, New Zealand; 2015.

- [12] Almesfer, N., Dizhur, D., Lumantarna, R., and Ingham, J. “Material Properties of Existing Unreinforced Clay Brick Masonry Buildings in New Zealand.” *Bulletin of the New Zealand Society for Earthquake Engineering*. 2014; 47(2).
- [13] ASTM International. ASTM C1314-11a: Standard Test Method for Compressive Strength of Masonry Prisms. West Conshohocken, Pennsylvania; 2011. Doi: 10.1520/C1314-11A.
- [14] The Masonry Society (TMS) Building Code Requirements and Specification for Masonry Structures, Boulder, Colorado, USA. 2011
- [15] Standards New Zealand (NZS). NZS 3112.2 Part 2: Tests Relating to the Determination of Strength of Concrete. Wellington, New Zealand, 1986.
- [16] Transit New Zealand. Transit New Zealand Bridge Manual. S. Stewart, Transit New Zealand and Opus International Consultants. Wellington, Transit New Zealand, c2004.
- [17] ACI (American Concrete Institute). ACI 209R-92: Prediction of Creep, Shrinkage, and Temperature Effects in Concrete Structures, 1992.
- [18] Priestley, M.J.N. (1996). “Displacement-based seismic assessment of existing reinforced concrete buildings.” *Bulletin of the New Zealand National Society for Earthquake Engineering*, 29(4), 256–272, [http://www.nzsee.org.nz/db/Bulletin/Archive/29\(4\)0256.pdf](http://www.nzsee.org.nz/db/Bulletin/Archive/29(4)0256.pdf).
- [19] NZSEE (New Zealand Society for Earthquake Engineering). Assessment and Improvement of the Structural Performance of Buildings in Earthquakes, Recommendations of a NZSEE Project Technical Group. Incorporated Corrigenda No. 1&2, Section 10, Seismic Assessment of Unreinforced Masonry Buildings, New Zealand Society for Earthquake Engineering, Wellington, New Zealand; 2006.
- [20] ASTM International. ASTM C109/C109M-13: Standard Test Method for Compressive Strength of Hydraulic Cement Mortars (Using 2-in. or [50-mm] Cube Specimens). West Conshohocken, Pennsylvania; 2013. Doi: 10.1520/C0109\_C0109M-13.
- [21] Lumantarna, R. Material Characterisation of New Zealand’s Clay Brick Unreinforced Masonry Buildings. Doctoral Dissertation, The University of Auckland, Auckland, New Zealand; 2012.
- [22] ASTM International. ASTM C67-11: Standard Test Methods for Sampling and Testing Brick and Structural Clay Tile. West Conshohocken, Pennsylvania; 2011. DOI: 10.1520/C0067-11.
- [23] ASTM International. ASTM C1531-09: Standard Test Methods for In Situ Measurement of Masonry Mortar Joint Shear Strength Index. West Conshohocken, Pennsylvania; 2009. DOI: 10.1520/C1531-09.
- [24] ASTM International. ASTM C1072-11: Standard Test Methods for Measurement of Masonry Flexural Bond Strength. West Conshohocken, Pennsylvania; 2011. DOI: 10.1520/C1072-11.
- [25] ASTM International. ASTM C39/C39M-14: Standard Test Method for Compressive Strength of Cylindrical Concrete Specimens. West Conshohocken, Pennsylvania; 2011. Doi: 10.1520/C0039\_C0039M-14A.

- [26] ASTM International. ASTM A370-12a: Standard Test Methods and Definitions for Mechanical Testing of Steel Products. West Conshohocken, Pennsylvania; 2012. Doi: 10.1520/A0370-12A.
- [27] ASCE (American Society of Civil Engineers). ASCE 41-13: Seismic evaluation and retrofit of existing buildings. Reston, Virginia; 2014.
- [28] Yi T., Moon F. L., Leon R.T., and Kahn L.F. "Flange effects on the nonlinear behaviour of URM piers." *The Masonry Society Journal*. 2008;26(2), 31-42.
- [29] Manie, J. and Kikstra, W. P. (Editors), (2014). "DIANA – Finite Element Analysis. User's Manual release 9.5" Published by TNO DIANA BV, Delftechpark 19a, 2628 XJ Delft, The Netherlands.
- [30] Bazant, Z.P., and Oh, B.H. "Crack band theory for fracture of concrete." *Material and Structures*, 1983;16:155–177.
- [31] CEB-FIP. Model Code 90, Thomas Telford Ltd., 1993.
- [32] EN 1996-1-1 (2005). "Eurocode 6: Design of masonry structures – Part 1-1: General rules for reinforced and unreinforced masonry structures". European Committee for Standardization (CEN), Brussels.
- [33] Rots, J.G. (Editor). "Structural masonry: An experimental/numerical basis for practical design rules." Balkema, 1997.
- [34] Van der Pluijm, R. "Non-linear Behaviour of Masonry under Tension." *Heron*, 1997; 42(1): 25-54.
- [35] Lourenco P. B., Barros J. O., Almeida J. C., (2002) "Characterization of masonry under uniaxial tension". GROW-1999-70420 "ISO-BRICK". University of Minho.
- [36] Lourenco, P.B. "Structural masonry analysis: recent developments and prospects," In: Proceedings of the 14th international brick & brick masonry conference, Sydney, Australia, 17–20 February; 2008; 1341–1356.
- [37] Deliverable D7, "Review of existing models for global response and local mechanisms". PERPETUATE Project, 2010.
- [38] Galasco, A., Lagomarsino, S., Penna, A., Cattari, S. "TREMURI program: Seismic Analyses of 3D Masonry Buildings". University of Genoa, 2009.
- [39] Turnsek V. and Cacovic F. "Some Experimental Results on the Strength of Brick Masonry Walls." 2nd International Brick and Block Masonry Conference, Stoke on Trent, UK; 1970.
- [40] *Norme Tecniche per le Costruzioni (NTC)*, Decreto Ministero delle Infrastrutture, 14 gennaio 2008, G.U. n. 29 del 4 febbraio 2008 - Suppl. Ordinario n. 30.  
[http://www.cslp.it/cslp/index.php?option=com\\_docman&task=doc\\_download&gid=3269&Itemid=10](http://www.cslp.it/cslp/index.php?option=com_docman&task=doc_download&gid=3269&Itemid=10) (In Italian).
- [41] Priestley, M. J. N., Calvi, G. M., and Kowalsky, M. J. (2007). "Displacement base seismic design of structures." IUSS Press. Fondazione Eucentre, Pavia, Italy.